Soomro *et al. Biochar* (2026) 8:105
https://doi.org/10.1007/s42773-026-00617-9

Biochar

ORIGINAL RESEARCH Open Access

Mechanism-resolved operating windows for biochar production from lavender distillation residue

Ahsanullah Soomro[1,2*], Anıl Tevfik Koçer[1,3], Mahdi Hassan[2,4] and Didem Balkanlı[1]

Abstract

Lavender distillation residue is an underutilized lignocellulosic carbon waste with strong potential for value-added conversion to biochar; however, pyrolysis operating windows are often selected using end-point product metrics alone, with limited mechanistic grounding and weak integration of energy and environmental burdens. Here, a 13-run N_2 pyrolysis design space (200–600 °C; 10–40 °C min^{-1}; 0–30 min hold) was evaluated to develop a mechanism-resolved operating-window framework coupling thermal fingerprints, conversion-dependent kinetics, and decision-oriented screening. Thermogravimetric analysis revealed heating-rate-dependent DTG peak migration ($T_{max} \approx$ 327 → 364 °C for 5 → 40 °C min^{-1}). DTG overlap was quantified using constrained multi-peak deconvolution with information-criterion selection, showing β-dependent statistical resolvability (two peaks at 5–10 °C min^{-1}; three peaks at 20–40 °C min^{-1}) consistent with overlap-limited separability rather than a literal reaction count. ICTAC-aligned isoconversional kinetics (KAS/FWO/Starink/Friedman) indicated regime evolution: apparent activation energies were comparatively stable through $\alpha = 0.1–0.6$ but increased sharply at high conversion ($\alpha = 0.9$), consistent with late-stage carbonization where derivative sensitivity increases. Across the matrix, final temperature exerted the dominant first-order control on the yield–carbonization trade-off. To translate mechanistic insight into actionable selection, electricity-normalized indicators and gate-to-gate EF3.0 midpoint burdens were integrated via entropy-weighted TOPSIS, identifying Run 5 as the best-compromise operating point (48.94% yield; 0.85 kWh kg^{-1} char; 2.05 kWh kg^{-1} fixed-C). Imposing an FC ≥ 60% constraint shifted the preferred option to Run 4 (61.67% fixed carbon; 8.16 kWh kg^{-1} fixed-C). Overall, the study provides a reproducible pathway from thermal fingerprinting to kinetic regime diagnosis and energy/LCA-informed operating-window selection, enabling defensible process design for lavender-residue biochar valorization.

Highlights

- Lavender residue was converted into useful biochar through controlled heating.
- Thermal analysis showed how heating conditions affect biochar formation.
- Energy and environmental checks helped select practical production conditions.

Keywords Lavender distillation residue, Pyrolysis, Thermogravimetric analysis (TGA/DTG), Isoconversional kinetics, Environmental footprint 3.0 (EF3.0) gate-to-gate life cycle assessment, EWM–TOPSIS (multi-criteria decision analysis)

*Correspondence:
Ahsanullah Soomro
ahsanullah.soomro@yildiz.edu.tr
Full list of author information is available at the end of the article

Springer

Graphical Abstract

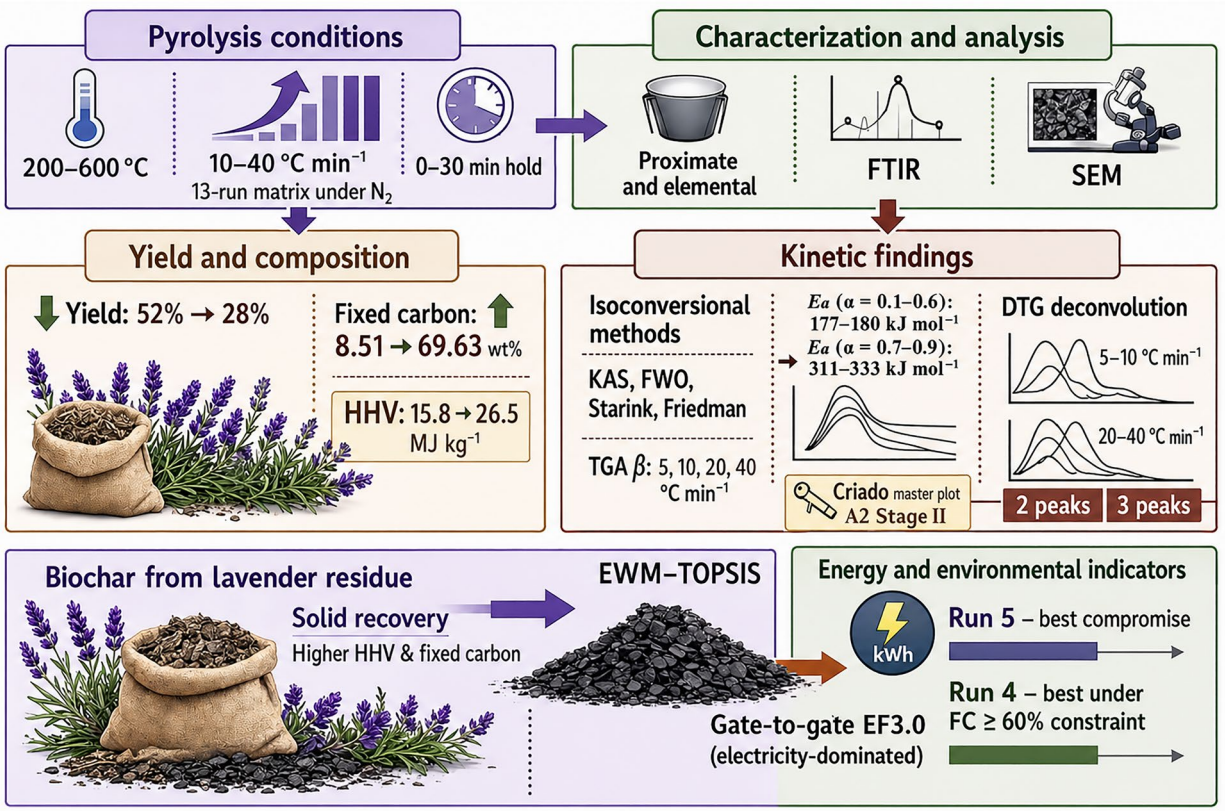

1 Introduction

The transition toward a circular bioeconomy is accelerating the valorization of agricultural and agro-industrial residues as secondary resources rather than disposal liabilities (Ravindiran et al. 2024). Among thermochemical conversion routes, pyrolysis is widely applied because it can process diverse biomass streams and generate a carbon-rich solid (biochar), condensable liquids (bio-oil), and non-condensable gases, with product distribution governed primarily by peak temperature, heating rate, and vapor/solid residence time. Biochar is often the most strategically important fraction because of its multifunctionality as a soil amendment, liming agent, long-term carbon-sequestration medium, renewable solid fuel, and versatile adsorbent for environmental pollutant removal (Ravindiran et al. 2024; Enebe et al. 2025; Parvari et al. 2025). However, translating these benefits into deployable systems requires process design supported by mechanistically interpretable and quantitatively auditable links between the heating program, decomposition structure, and conversion-dependent kinetics—rather than relying solely on end-point product metrics. In this sense, "operating windows" should be defined not only by what the product is, but also by why the product forms under a given thermal history. From a sustainability perspective, this work is particularly relevant to United Nations Sustainable Development Goals (SDGs) 7 (Affordable and Clean Energy), 12 (Responsible Consumption and Production), and 13 (Climate Action), as it advances renewable biomass utilization, supports responsible residue valorization within a circular-bioeconomy framework, and incorporates energy- and environment-related criteria into process selection.

Lavender (Lavandula spp.) is a high-value aromatic crop cultivated for essential oils used in fragrance, food, and medicinal industries. Europe remains a major production region, and global annual production of true lavender (Lavandula angustifolia Mill.) essential oil has been estimated at approximately 300–500 tons (Crișan et al. 2023). Because fresh lavender biomass contains only about 0.8–1.3% essential oil, steam distillation inherently generates a substantially larger quantity of residual solid

biomass (distilled straw/stalk material) than the final oil product (Barar and Bensebia 2025). These residues are frequently burned, landfilled, or diverted to low-value composting despite retaining a lignocellulosic framework and residual bioactive fractions (Karagianni et al. 2025). Valorization routes for aromatic-plant distillation residues have begun to emerge, including gasification studies on oregano and lavender residues (Yılmaz Çinçin et al. 2025) and hydrothermal carbonization of distilled lavender stalks (Li et al. 2023a). Nevertheless, systematic assessments that translate lavender-residue thermal conversion data into mechanistically anchored evidence for defining pyrolysis operating windows—and for anticipating carbonization behavior under practical heating programs—remain limited. Published work on lavender and related aromatic residues has often emphasized structural characterization, application screening, or analytical pyrolysis (e.g., Py-GC/MS) (Lesage-Meessen et al. 2018), which is valuable for compositional insight but does not directly provide conversion-resolved kinetic evidence usable for operating-window design, leaving a gap in TGA-grounded interpretation that is explicitly process-relevant.

For biomass residues broadly, severity effects are well established: increasing peak temperature typically decreases char yield while increasing fixed carbon and aromaticity, reflecting progressive devolatilization and carbonization (Atinafu et al. 2025). Studies on other aromatic herbs such as rosemary further show that plant fraction (leaves versus stems) and applied thermal severity can substantially alter biochar physicochemical properties and energy content (Dira et al. 2024). These macroscopic trends, however, do not resolve kinetic heterogeneity during non-isothermal conversion. Thermogravimetric analysis (TGA) commonly reveals overlapping regimes, including dehydration, active devolatilization, and a slower high-conversion region associated with char formation, structural rearrangement, and progressive carbonization of the residual solid (Yang et al. 2007). Accordingly, the ICTAC Kinetics Committee recommends model-free (isoconversional) approaches for evaluating conversion-dependent apparent activation energies in complex multi-step thermal decomposition systems, because such methods avoid imposing a single global reaction model on inherently heterogeneous processes (Koga et al. 2023). The Flynn-Wall-Ozawa (FWO) and Kissinger-Akahira-Sunose (KAS) methods are among the most widely applied isoconversional approaches in biomass pyrolysis and frequently provide robust conversion-dependent activation-energy trends across broad conversion ranges (Shrivastava et al. 2025). Model-fitting analyses can provide additional interpretive context; however, ICTAC cautions that single-step fits can yield biased kinetic triplets when inherently multi-step behavior is compressed into one mechanism and therefore should be interpreted against an isoconversional baseline (Khawam and Flanagan 2006; Koga et al. 2023). A complementary challenge is that strongly overlapped DTG features can mask stage structure, making it difficult to attribute how much of the overall mass-loss trajectory is governed by distinct sub-processes under different heating programs.

A second, often overlooked, limitation concerns how "optimum" biochar conditions are selected. Many studies tune thermal parameters (temperature, heating rate, residence time) and prioritize product-oriented metrics (Koçer and Özçimen 2022; Koçer et al. 2023, 2024, 2020; Özçimen and Ersoy-Meriçboyu 2010), while process energy demand and associated environmental burdens are not included in the decision basis (Desjardins et al. 2024; Gamaralalage et al. 2025). This omission is consequential because increasing severity can improve carbon quality while simultaneously increasing electricity intensity and shifting the overall sustainability profile (e.g., climate-change and resource-use indicators). For value-added processing of carbon waste, selection criteria that ignore energy and environmental burdens risk identifying "optima" that are not deployable at scale. To address this gap, an entropy-weighted TOPSIS (EWM–TOPSIS) framework is introduced here to jointly evaluate biochar performance together with energy- and environment-related indicators, enabling a transparent compromise ranking across competing objectives and strengthening the defensibility of the selected operating condition. Importantly, this approach also allows explicit quality constraints (e.g., minimum fixed carbon) to be tested, rather than implicitly assumed.

Building on these needs, this work advances a mechanism-resolved, data-auditable analysis framework for lavender distillation residues that connects pyrolysis conditions to both product outcomes and conversion-dependent kinetic structure. The framework combines: (i) information-criterion screening of DTG complexity to resolve overlapping decomposition features beyond the moisture domain, (ii) quantitative partitioning of chemical-stage contributions to demonstrate how decomposition structure evolves with the heating program, and (iii) regime-wise interpretation of $Ea(\alpha)$ to identify late-conversion kinetic escalation that is commonly obscured by single-mechanism summaries. By integrating these kinetic insights with a multi-criteria operating-window selection step that explicitly includes energy and environmental decision factors, the study moves beyond condition-based narratives toward transferable, process-relevant evidence for defining pyrolysis operating

windows for lavender residues within circular bioeconomy strategies.

2 Materials and methods

2.1 Biomass collection and biochar production

Lavender distillation residue was obtained from a farm in Çanakkale, Türkiye. During harvest at peak flowering, the aerial biomass was cut approximately 5 cm below the inflorescence. Flowers were used for essential-oil production, and the post-distillation solid residue was retained as the feedstock for biochar production and subsequent characterization. The residue was oven-dried at 70 °C for 24 h, homogenized, and stored in sealed containers prior to thermochemical experiments. Biochar was produced using a Protherm tubular furnace equipped with an inert-gas supply and PID temperature control (Honeywell). For each bench-scale pyrolysis run in the tubular furnace, approximately 1.0 g of dried lavender residue was placed in a ceramic crucible and positioned in the reactor hot zone. Prior to heating, the furnace chamber was purged with high-purity N_2 for 15 min to remove residual oxygen. Pyrolysis was then conducted under continuous N_2 flow (≈ 300 mL min^{-1}) to maintain oxygen-limited conditions and prevent oxidative degradation during heating and cooling. A structured 13-run experimental matrix was implemented to evaluate the effects of temperature (200, 400, 600 °C), heating rate (10, 25, 40 °C min^{-1}), and retention time at peak temperature (0–30 min) on biochar formation. The complete run matrix is visualized in Fig. 1, where individual runs are mapped as heating rate versus retention time within temperature panels and labelled by run number for direct traceability. After reaching the target temperature at the specified heating rate, samples were held isothermally for the assigned retention time (0, 15, or 30 min), after which the furnace was switched off and allowed to cool naturally to room temperature under continuous N_2 flow. Upon cooling, the resulting biochar was recovered and weighed for yield determination, and the samples were stored in airtight containers for subsequent physicochemical characterization (including fixed carbon determination using ASTM-based proximate analysis, as described in Sect. 2.2).

EWM–TOPSIS was used as a decision-support tool to move beyond single-metric rankings (energy-only or LCIA-only) and to provide a transparent, reproducible compromise selection that simultaneously accounts for product performance (yield and fixed carbon) and burdens (electricity intensity and EF3.0 midpoints) (Behzadian et al. 2012; Chen 2021). Here, electricity intensity refers to the specific electricity consumption (SEC) of the pyrolysis process, expressed as kWh kg^{-1} biochar and kWh kg^{-1} fixed C, rather than to the heat content of the biochar itself. The electrical energy input was estimated as an upper-bound from the furnace rated power and the programmed process time (heating plus hold time), and was then normalized on a 1.0 kg dry-feed basis using the measured biochar yield and fixed-carbon content, as detailed in Supplementary File S1. While the EF3.0 categories in this gate-to-gate model show largely parallel variation—so a footprint-minimization ranking can be inferred directly from electricity demand—EWM–TOPSIS adds value by quantifying trade-offs and identifying cases where higher product recovery can offset modest increases in burden, thereby changing the relative order of some runs. The approach therefore complements the direct energy/LCA screening by formalizing multi-objective selection and confirming the best-compromise optimum through a single closeness coefficient C_i(details in Supplementary Files S1 and S2).

2.2 Thermogravimetric analysis and kinetic theory

Thermogravimetric analysis (TGA) was carried out using a TA Instruments SDT Q600 under a high-purity N_2 atmosphere (99.99%, 50 mL min^{-1}) to investigate the thermal decomposition behavior of lavender distillation residue under pyrolytic conditions. For each TGA

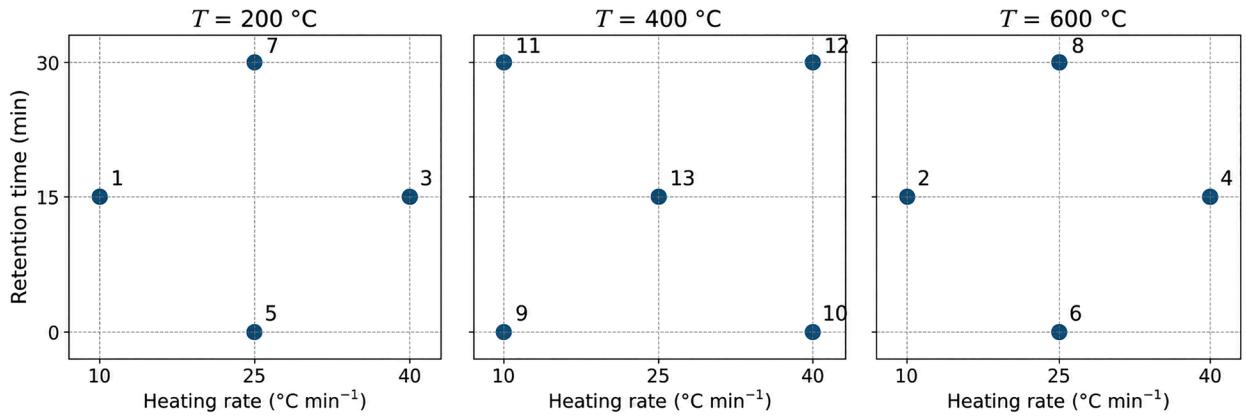

Fig. 1 Experimental run matrix for lavender-residue pyrolysis (13 runs)

run, approximately 5 mg of dried lavender biomass was loaded into an alumina crucible for thermal decomposition analysis under controlled non-isothermal conditions. Measurements were conducted under an inert nitrogen atmosphere (50 mL min^{-1}) by heating from ambient temperature to 700 °C at heating rates of 5, 10, 20, and 40 °C min^{-1}. To quantify the kinetic response without imposing a single global reaction model, model-free isoconversional methods were applied to estimate the apparent activation energy as a function of conversion, $Ea(\alpha)$. This approach is aligned with ICTAC recommendations for kinetic analysis of complex solid-state decomposition systems, in which conversion-dependent evaluation is preferred over fitting a single global mechanism to inherently multi-step behavior (Koga et al. 2023). In this study, "ICTAC-aligned" therefore denotes the use of conversion-dependent, model-free kinetic analysis as a diagnostic framework, rather than a claim of a single mechanistic solution. Among these, the Kissinger-Akahira-Sunose (KAS) (Akahira and Sunose 1971; Kissinger 1957), Flynn-Wall-Ozawa (FWO) (Flynn and Wall 1966; Ozawa 1965), Starink (Starink 1996), and Friedman (Friedman 1964) methods were employed. In these methods, the temperature-conversion rate data were used to construct linear plots, and the activation energy (Ea) values were calculated from the slopes of these plots. The equations for the model-free methods used in this study are shown below:

- KAS method:

$$ln\left(\frac{\beta}{T^2}\right) = lnln\left(\frac{AE}{Rg(\alpha)}\right) - \frac{E}{RT} \quad (1)$$

- FWO method:

$$ln\beta = lnln\left[\frac{A.E}{R.g(\alpha)}\right] - 5.331 - 1.052\frac{E}{R.T} \quad (2)$$

- Starink method:

$$ln\left(\frac{\beta}{T^{1.92}}\right) = Constant - 1.0008\frac{E}{RT} \quad (3)$$

- Friedman method:

$$ln\left(\beta\frac{d\alpha}{dT}\right) = lnln\left(A.f(\alpha)^n\right) - \frac{E}{RT} \quad (4)$$

In these equations, β, α, and T represent the heating rate (K min^{-1}), conversion rate, and temperature (K), respectively. A, E, and R represent the frequency factor (min^{-1}), apparent activation energy (J mol^{-1}), and universal gas constant (8.314 J mol^{-1} K^{-1}), respectively. $f(\alpha)$ represents the reaction mechanism function, and $g(\alpha)$ represents the integral of $1/f(\alpha)$. The parameter n in the Friedmann equation represents the extent of reaction.

To resolve overlapping devolatilization regimes, DTG rate signals in the 150–500 °C window were deconvolved using a baseline-corrected Gaussian-mixture representation of the non-negative rate magnitude, with $n = 2$ and $n = 3$ candidate peak sets tested (Rego et al. 2019). The preferred peak number was selected quantitatively using residual sum of squares (RSS) together with Akaike and Bayesian information criteria (AIC/BIC), so that peak partitioning was based on both goodness-of-fit and model parsimony (Akaike 2003; Ferfari et al. 2025; Schwarz 1978). Stage contributions were then defined from the analytical area of each retained fitted peak and expressed as normalized fractions of the total fitted area, with fitted components ordered by increasing peak-center temperature (μ) and reported as Stage I–III. In this study, these stage fractions are interpreted as phenomenological contributions to the DTG devolatilization profile rather than as direct one-to-one assignments of discrete elementary chemical reactions. Mechanism screening was supported by the reduced Criado master-plot normalized at $\alpha = 0.5$, comparing experimental $(d\alpha/d\theta)/(d\alpha/d\theta)_{\alpha=0.5}$ with theoretical $f(\alpha)/f(0.5)$ curves for candidate models (Gotor et al. 2000). Details of model selection (RSS, AIC, BIC), stage fractions, fitted parameters, stage-boundary definitions, implementation descriptors, experimental master-plot values, model ranking, and experimental–theoretical comparisons are provided in Supplementary File S3 (Tables S5–S8 and S10–S13).

2.3 Characterization of biochar samples

To characterize the lavender residue and biochar after essential oil extraction under determined optimal pyrolysis conditions, FTIR spectroscopy, scanning electron microscopy (SEM), and real-time analysis were performed. In addition, the elemental compositions and higher heating values (HHV) of the samples were estimated based on the proximate analysis results. A Bruker Alpha FTIR spectrometer was used to identify surface functional groups in the raw lavender residue and the produced biochars. Spectra were recorded in ATR mode (32 scans) over 4000–500 cm^{-1} at a resolution of 4 cm^{-1}. The FTIR profiles were used to assess changes in the lignocellulosic structure after pyrolysis and the emergence or loss of key functional groups. A Zeiss EVO® LS 10 scanning electron microscope (SEM) was used to examine the surface morphology and structural aspects. Proximate analysis (moisture, volatile matter, ash, and fixed carbon) was conducted using a TA Instruments SDT Q600 thermogravimetric analyzer (TGA) following the thermogravimetric procedure described by García et al.

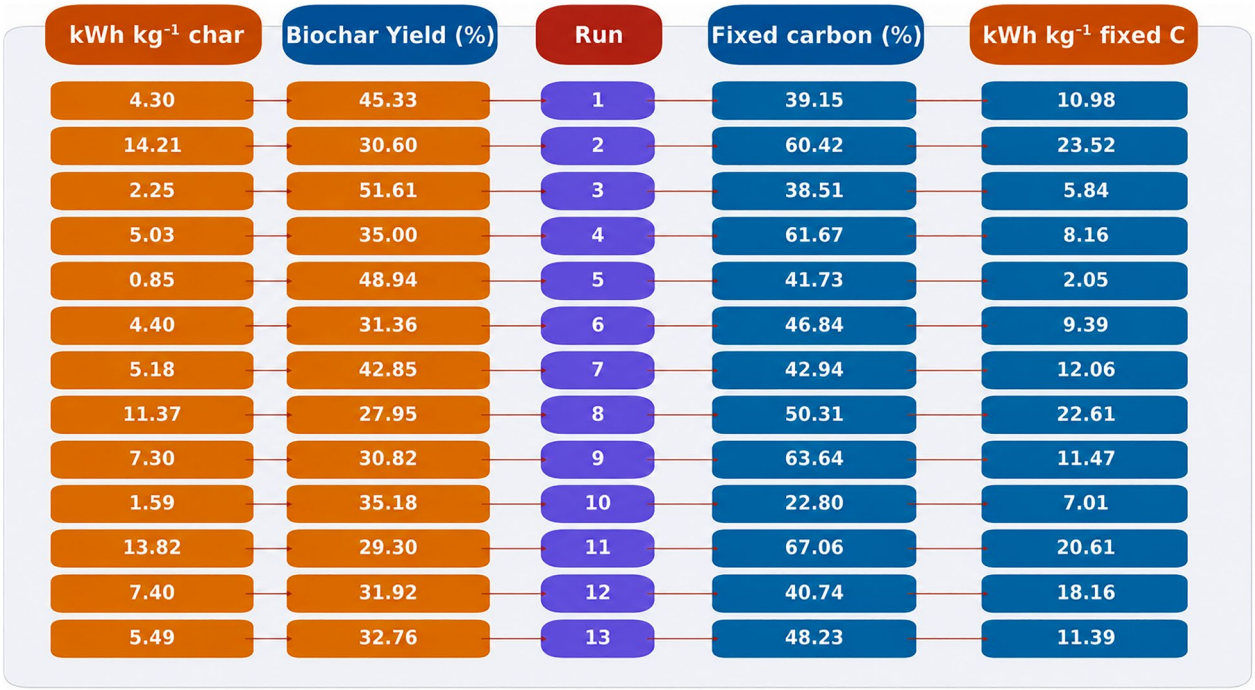

Fig. 2 Lavender-residue pyrolysis outcomes across the 13-run matrix, showing biochar yield, fixed-carbon content, and electricity intensity

(2012); volatile matter determination was referenced to ASTM E872, and fixed carbon was calculated by difference. The elemental composition and higher heating value (HHV) were calculated using the empirical correlations outlined in Nhuchhen (2016), Poomsawat and Poomsawat (2021), and Parikh et al. (2005), as shown below:

$$C(\%) = -35.9972 + 0.7698VMC + 1.3269FCC + 0.3250AC \quad (5)$$

$$H(\%) = 55.3678 - 0.4830VMC - 0.5319FCC - 0.5600AC \quad (6)$$

$$O(\%) = 223.6805 - 1.7226VMC - 2.2296FCC - 2.2463AC \quad (7)$$

$$N(\%) = 100 - (C + H + O + AC) \quad (8)$$

$$HHV(\text{MJ kg}^{-1}) = 0.1559VMC + 0.3536FCC - 0.0078AC \quad (9)$$

3 Results and discussion

Figure 2 consolidates biochar yield, fixed-carbon content, and electricity intensity (kWh kg^{-1} char; kWh kg^{-1} fixed C) across the explored pyrolysis matrix (200–600 °C; 10–40 °C min^{-1}; 0–30 min). Within the tested range, peak temperature exerted the strongest first-order control on the yield–carbonization trade-off. Increasing the final temperature from 200 to 600 °C at a constant 15 min residence time reduced yield while enriching fixed carbon: at 10 °C min^{-1}, yield decreased from 45.33% to 30.60% while fixed carbon increased from 39.15% to 60.42% (Runs 1–2); at 40 °C min^{-1}, yield decreased from 51.61% to 35.00% while fixed carbon increased from 38.51% to 61.67% (Runs 3–4), consistent with enhanced devolatilization and progressive carbonization under higher thermal severity (Koçer et al. 2023; Lindstrom et al. 2024). Heating-rate effects were condition-dependent, indicating that β influences outcomes primarily through the realized time–temperature pathway rather than acting as a standalone severity descriptor. This is most apparent at 400 °C without holding, where increasing β from 10 to 40 °C min^{-1} increased yield (30.82% → 35.18%) but coincided with a pronounced reduction in fixed carbon (63.64% → 22.80%) (Runs 9–10), suggesting that constrained exposure can limit effective carbonization at intermediate setpoints (Fraga et al. 2020; Zhu et al. 2021). Residence time further intensified carbonization under intermediate conditions; extending the hold from 0 to 30 min at 400 °C (10 °C min^{-1}) increased fixed carbon from 63.64% to 67.06% with a minor yield penalty (30.82% → 29.30%) (Runs 9 and 11).

Table 1 Gate-to-gate EF 3.0 midpoint results for lavender-residue pyrolysis runs ($n = 13$) based on run-specific electricity demand in openLCA

Run	Climate change (kg CO_2-eq)	Resource use, fossils (MJ)	Water use (m^3 depriv.)	Acidification (mol H^+ eq)	Photochem. ozone (kg NMVOC eq)
1	0.932101	10.295852	0.639446	0.004372	0.001777
2	2.079302	22.967671	1.426457	0.009754	0.003963
3	0.555676	6.137912	0.381208	0.002607	0.001059
4	0.842476	9.305867	0.577961	0.003952	0.001606
5	0.200760	2.217568	0.137727	0.000942	0.000383
6	0.659641	7.286296	0.452531	0.003094	0.001257
7	1.061161	11.721432	0.727985	0.004978	0.002023
8	1.520042	16.790159	1.042790	0.007130	0.002897
9	1.075501	11.879830	0.737823	0.005045	0.002050
10	0.268875	2.969957	0.184456	0.001261	0.000512
11	1.935902	21.383694	1.328081	0.009081	0.003690
12	1.129276	12.473821	0.774714	0.005297	0.002152
13	0.860401	9.503864	0.590258	0.004036	0.001640

The EF3.0 midpoint results across the 13 runs (Table 1) show a coherent, near-parallel response across the five indicators reported (climate change, fossil resource use, water use, acidification, and photochemical ozone formation). Such co-variation is commonly observed when a shared upstream contributor dominates multiple impact pathways within the defined system boundary, such that operating-condition changes largely scale that contributor rather than shift the hotspot structure. This hotspot-oriented interpretation aligns with LCIA practice, where co-variation patterns are used for decision-relevant interpretation rather than implying independent narratives for each category (Schomberg et al. 2022). In recent biochar LCAs, energy provision during conversion and post-processing has been identified as an important driver of greenhouse-gas emissions and overall environmental performance, supporting this interpretation for the present gate-to-gate mode (Desjardins et al. 2024; Gamaralalage et al. 2025).

To integrate experimental performance with electricity intensity and EF3.0 burdens in a single decision framework, an entropy-weighted TOPSIS (EWM–TOPSIS) model was applied to the 13-run matrix using eight criteria: yield and fixed carbon as benefit criteria, and kWh kg^{-1} fixed C together with five EF3.0 midpoint indicators as cost criteria. Entropy weighting assigns higher importance to criteria that provide greater discrimination across the dataset. In this matrix, yield received the largest weight (0.2396), followed by kWh kg^{-1} fixed C (0.1385) and fixed carbon (0.0868), while the EF3.0 indicators carried nearly equal weights (≈0.107 each) (Table 1). The TOPSIS closeness coefficients (C_i) provide the integrated run ranking (Table S2): Run 5 achieved the highest score ($C_i = 0.8612$) and was therefore identified as the best-compromise optimum under the selected criteria set, followed by Run 3 ($C_i = 0.8129$) and Run 1 ($C_i = 0.6395$). The lowest-ranked conditions were Run 2 ($C_i = 0.1835$) and Run 11 ($C_i = 0.2133$), reflecting their combined disadvantage across electricity intensity and midpoint burdens within the integrated scoring framework. Because optimum selection is constraint-dependent, a quality-constrained interpretation was also evaluated: when fixed carbon ≥ 60% is required (Runs 2, 4, 9, and 11), the best-compromise optimum within this feasible subset shifted to Run 4 (highest C_i within the constrained set), providing a defensible selection under a high-carbon requirement.

3.1 Characterization of biomass and biochar samples

Figure 3 evidences a pronounced compositional upgrading of lavender biomass to a carbon-enriched biochar after pyrolysis, consistent with the devolatilization–carbonization pathway of lignocellulosic solids. Proximate analysis shows an extensive loss of volatile matter (82.36 → 12.73 wt%, − 85%) accompanied by a sharp rise in fixed carbon (8.51 → 69.63 wt%, + 718%), reflecting extensive devolatilization with evolution of gaseous/condensable products (e.g., CO, CO_2, CH_4 and tar vapors) and progressive condensation of the residual solid into a more recalcitrant carbon matrix (Syguła et al. 2024; Zhang et al. 2020). The ash fraction nearly doubled (9.13 → 17.64 wt%, + 93%), as expected from preferential volatilization of organics and consequent concentration of inorganic minerals in the remaining solid (Zhang et al.

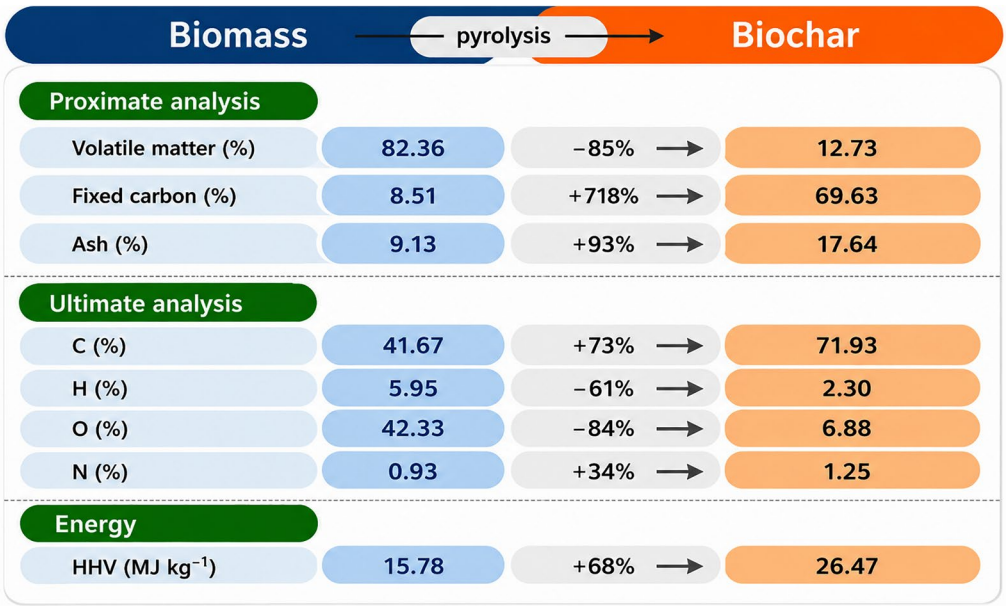

Fig. 3 Proximate and ultimate analysis and higher heating value (HHV) of raw lavender biomass and the corresponding biochar

2020). Enhanced aromatic condensation and removal of oxygen-containing functional groups during pyrolysis further support fixed-carbon enrichment and improved structural stability of the char matrix (Li et al. 2023b).

Ultimate analysis corroborates strong deoxygenation and carbon densification: carbon increased from 41.67 to 71.93 wt% (+73%), while hydrogen and oxygen decreased from 5.95 to 2.30 wt% (−61%) and from 42.33 to 6.88 wt% (−84%), respectively. These shifts translate into substantially lower atomic H/C (≈1.71 → 0.38) and O/C (≈0.76 → 0.07) ratios, indicating formation of a more condensed and persistent carbon structure; notably, the product falls within commonly cited stability thresholds (H/C < 0.4 and O/C < 0.2) for highly carbonized biochars (Oginni and Singh 2020). Nitrogen increased modestly (0.93 → 1.25 wt%, +34%), consistent with concentration during mass loss and partial retention/incorporation of thermally stable N-bearing functionalities under oxygen-limited conditions (Li et al. 2023b). These compositional changes are mirrored by the energy metric: HHV increased from 15.78 to 26.47 MJ kg^{-1} (+68%), consistent with carbon enrichment and substantial oxygen depletion, which reduce the dilution of heating value by oxygenated functionalities and increase energy density on a mass basis(Koçer et al. 2024). Overall, the results confirm that lavender residue pyrolysis yields a low-volatility, carbon-rich solid with elevated ash concentration and markedly improved fuel characteristics.

Scanning electron microscopy (SEM) was employed to examine the surface morphology and microstructural evolution of the raw lavender biomass and the corresponding biochar. Representative SEM images are presented in Fig. 4. Figure 4a shows that the original biomass surface was dense and the fibrous structure was partially preserved. No pores were observed and the structure was dense, indicating that the lignocellulose components (cellulose, hemicellulose, and lignin) in the biomass formed a tightly bound matrix before pyrolysis. In addition, some small surface protrusions were also observed, corresponding to inorganic particles such as calcium or silicon dioxide residues—a typical morphological feature of agricultural residues(Montoya et al. 2017). In contrast, the image of biochar (Fig. 4b) shows that its structure was significantly more porous after pyrolysis. Although the overall cellular structure of the biomass was largely preserved, the cell walls were thinned and even completely collapsed in some areas. This transformation was due to the release of volatile compounds, leaving hollow cell spaces and a stable carbon skeleton. A large number of micropores and mesopores were present on the surface of the biochar, which can be attributed to the pressure difference generated during the escape of the gas phase and tar phase(Cai et al. 2023). This porous morphology is beneficial for adsorption, catalyst support and ion exchange applications (Su et al. 2024).

Figure 5 shows the FTIR spectra of lavender biomass and its biochar. The spectra confirm a marked shift from an oxygenated lignocellulosic matrix toward a more carbonized structure dominated by condensed aromatic domains. In the biomass spectrum, the

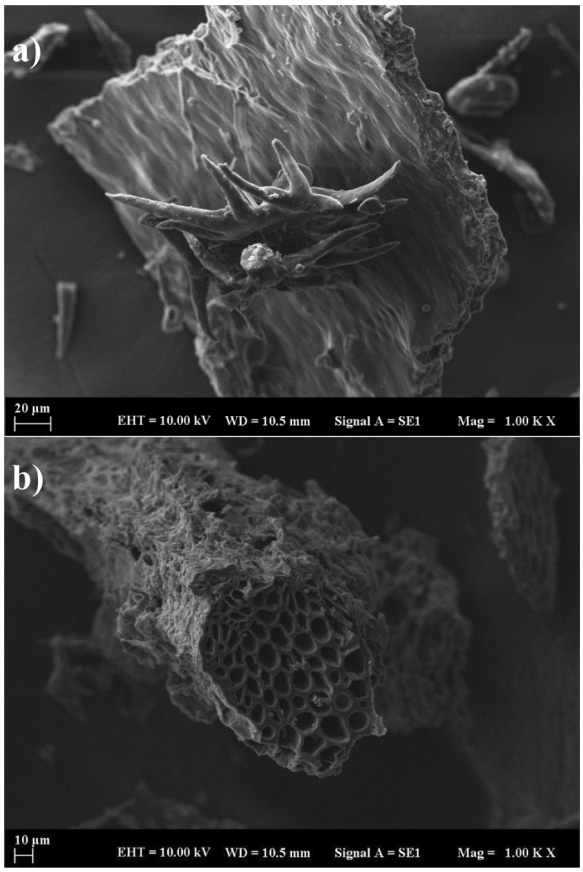

Fig. 4 SEM images of **a** waste lavender biomass and **b** biochar produced under optimized pyrolysis conditions

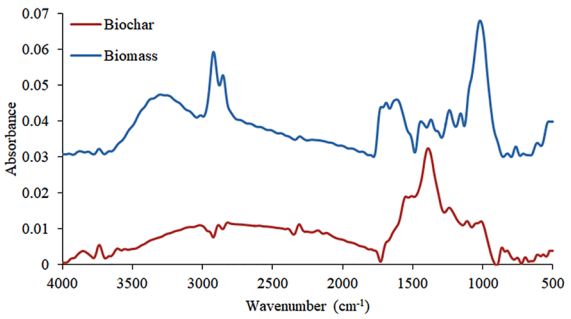

Fig. 5 FTIR spectra of lavender biomass and biochar produced under optimized pyrolysis conditions

broad band at 3400–3500 cm^{-1} corresponds to O–H stretching of hydroxyl groups and adsorbed moisture (Permana et al. 2024). The band near 2920 cm^{-1} represents aliphatic C–H stretching, while the peak around 1730 cm^{-1} is associated with carbonyl (C=O) groups in carboxylic acids/esters and related oxygenates (Logeshwari et al. 2024). The region 1600–1500 cm^{-1} reflects aromatic C=C skeletal vibrations, and bands between 1200 and 1000 cm^{-1} are attributed to C–O–C/C–O stretching typical of cellulose, hemicellulose, and lignin structures (Tariq et al. 2024).

After pyrolysis, these oxygen- and hydrogen-bearing functionalities weaken substantially. The reduction of the O–H band indicates dehydration and removal of hydroxyl-bearing moieties during carbonization. Similarly, attenuation of the aliphatic C–H band reflects cleavage of long-chain aliphatic structures and volatilization of light hydrocarbons and oxygenates (Sharma et al. 2024). The strong suppression of the carbonyl region (~ 1730 cm^{-1}) evidences decarboxylation/decarbonylation and loss of oxygenated groups such as carboxyl, ester, and aldehyde functionalities(Chu et al. 2017). In contrast, the aromatic skeletal region becomes relatively more prominent, consistent with progressive condensation and growth of polyaromatic structures during pyrolysis (Zhang et al. 2025). Quantitatively, baseline-corrected band-area integration indicates enhanced aromatization and deoxygenation in the optimized-run biochar. The aromatic skeletal region (1620–1500 cm^{-1}) increased from 0.100 to 0.193 (≈ 1.93×), while oxygenated functional regions decreased sharply: the carbonyl band (1750–1680 cm^{-1}) dropped from 0.144 to 0.00174 (≈ 98.8% reduction), and the C–O band (1260–1000 cm^{-1}) decreased from 0.151 to 0.0338 (≈ 78% reduction). The aliphatic C–H region (2950–2850 cm^{-1}) also decreased from 0.296 to 0.0336 (≈ 89% reduction), collectively indicating conversion from oxygenated/aliphatic biomass to a more condensed aromatic carbon matrix consistent with elevated fixed carbon content (Chu et al. 2017; Koçer and Özçimen 2022; Sharma et al. 2024; Zhang et al. 2025). Baseline-corrected FTIR peak heights, band areas, and derived indices used for semi-quantitative comparison are summarized in Supplementary File S3 (Tables S1–S3).

3.2 Thermogravimetric analysis of lavender wastes

Figure 6 presents the TG and DTG responses of raw lavender distillation residue measured at $\beta = 5$, 10, 20, and 40 °C min^{-1}, confirming the multi-stage thermal decomposition typical of lignocellulosic solids. The initial mass loss below ~ 100 °C is attributed to evaporation of free and bound moisture (Agrawal and Chakraborty 2013). The main devolatilization region occurs predominantly within ~ 200–400 °C, where hemicellulose and cellulose decompose rapidly with partial overlap, while lignin contributes more gradually over a broader temperature interval (Yang et al. 2007). Above ~ 400 °C, the mass-loss rate decreases markedly as char-forming reactions and solid-phase rearrangements become dominant, and the remaining mass at 700 °C corresponds to a thermally stable carbonaceous residue with mineral ash.

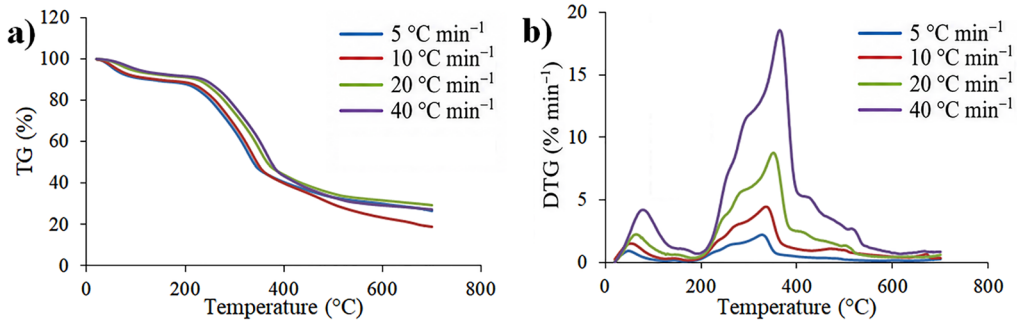

Fig. 6 **a** TG and **b** DTG curves of lavender biomass at different heating rates (5, 10, 20, and 40 °C min^{-1}).

The DTG maximum shifts systematically with heating rate (T_{max} = 327, 335, 351, and 364 °C for β = 5, 10, 20, and 40 °C min^{-1}, respectively; Supplementary File S3, Table S4), consistent with finite-rate non-isothermal effects (thermal lag and heat/mass transfer limitations) under faster heating. Directly comparable non-isothermal N_2-pyrolysis TGA studies reporting T_{max} values specifically for raw lavender distillation residue are limited. Nevertheless, the present T_{max} range (327–364 °C) agrees well with the established pyrolytic behavior of lignocellulosic and herbaceous biomass, for which the principal DTG maximum is typically located in the main devolatilization region governed by overlapping hemicellulose and cellulose decomposition, while progressively shifting to higher temperature with increasing heating rate because of thermal lag and heat/mass-transfer limitations (Fraga et al. 2020; Yang et al. 2007). Thus, the systematic upward migration of T_{max} observed here is consistent with the expected non-isothermal response of biomass feedstocks and supports assignment of these peaks to the dominant devolatilization stage of lavender distillation residue rather than to anomalous thermal behavior. When reported as d(TG)/dt, the peak intensity increases strongly with β (DTGmax = 2.211–18.570% min^{-1}, Table S4); however, after conversion to a temperature basis using d(TG)/dT = (d(TG)/dt)/β, the peak magnitude remains comparatively similar (0.4379–0.4643% $°C^{-1}$; Table S4), indicating that much of the apparent intensification in % min^{-1} reflects scaling with β rather than a proportional increase per degree. The dominant-peak width is likewise broadly stable (FWHM = 102.66–110.79 °C; Table S4). At high temperature, TG trajectories converge but retain modest differences in residue at 700 °C (18.86–29.31 wt%; Table S4), consistent with the combined influence of heating program and lignin-associated slow decomposition on final solid fraction (Chen et al. 2023; Koçer et al. 2023). A consolidated TG/DTG fingerprint dataset (T_5, T_{10}, T_{50}, T_{max}, DTGmax in % min^{-1} and % $°C^{-1}$, FWHM, and residue at 700 °C) is provided in Supplementary File S3 (Table S4).

3.3 Kinetic and mechanism-resolved interpretation

Conversion-dependent activation energies, $Ea(\alpha)$, were determined using four model-free isoconversional methods (KAS, FWO, Starink, and Friedman) (Fig. 7), with complete datasets reported in Supplementary File S3 (Table S9). The variation of Ea with α indicates overlapping steps rather than a single global mechanism. Over α = 0.1–0.6, Ea remains comparatively stable with strong linearity for KAS/FWO/Starink ($R^2 \approx$ 0.985–0.995; Table S9), spanning Ea = 172.912–182.801 kJ mol^{-1}, while Friedman yields Ea = 175.588–191.744 kJ mol^{-1} and shows greater sensitivity to derivative-signal variability (Table S9). Here, "late-stage kinetics" refers to the high-conversion region of the pyrolysis trajectory, where the more reactive fractions have largely decomposed and the remaining mass loss increasingly reflects carbonization and structural rearrangement of the residual solid. A clear regime change appears at higher conversion: at α = 0.7, Ea increases (KAS/FWO/Starink: 187.446–188.175 kJ mol^{-1}; Friedman: 203.787 kJ mol^{-1}) and Friedman linearity deteriorates (R^2 = 0.732; Table S9). At α = 0.8–0.9, Ea escalates sharply, reaching 260.615–263.335 kJ mol^{-1} (α = 0.8) and 484.878–498.137 kJ mol^{-1} (α = 0.9) for KAS/FWO/Starink and 290.822 (α = 0.8) and 504.230 kJ mol^{-1} (α = 0.9) for Friedman (Table S9); in this regime, rates are low and derivative-based estimates become more sensitive to signal noise and evolving structural/transport constraints(Porcu et al. 2021; Shrivastava et al. 2025; Wang et al. 2018). Average Ea over α = 0.1–0.9 is 223.328 (KAS), 221.922 (FWO), 223.554 (Starink), and 231.061 kJ mol^{-1} (Friedman) (Table S9). These activation-energy levels are within the range reported for lignocellulosic biomass pyrolysis, although the high-conversion region in the present study shifts toward markedly higher values. For example, non-isothermal isoconversional analysis of sugarcane bagasse reported

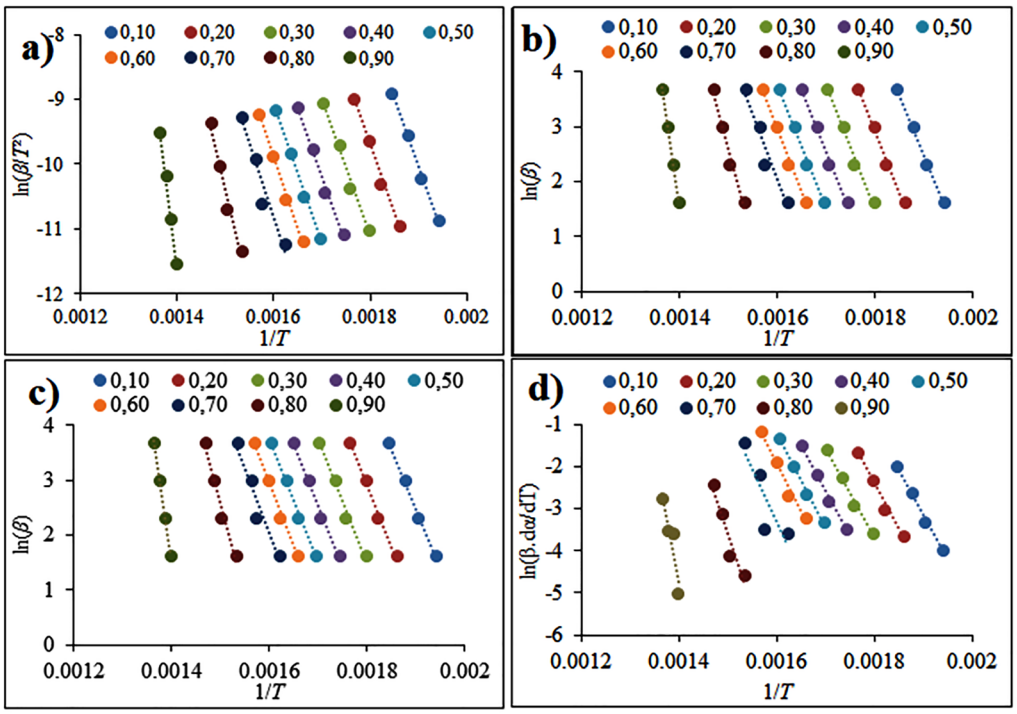

Fig. 7 Isoconversional plots for lavender biomass pyrolysis obtained using **a** KAS, **b** FWO, **c** Starink, and **d** Friedman methods

apparent activation energies of 165–180 kJ mol^{-1} over the 0.1–0.8 conversion range (Aboyade et al. 2013). In the present study, the more stable mid-conversion region ($\alpha = 0.1–0.6$) gave Ea values of 173–183 kJ mol^{-1} for KAS/FWO/Starink and 176–192 kJ mol^{-1} for Friedman, which are broadly consistent with that reported range. By contrast, the full-range averages (221.9–231.1 kJ mol^{-1}) are elevated by the sharp *E*a increase at $\alpha = 0.8–0.9$, indicating relatively stronger resistance during the late stages of conversion, consistent with progressive carbonization and structural rearrangement.

To quantify DTG peak overlap and assess whether the devolatilization region is more parsimoniously represented by two or three sub-processes, DTG curves were deconvoluted using constrained multi-peak functions and evaluated by RSS together with AIC and BIC (Supplementary File S3, Table S5). Because AIC/BIC penalize added degrees of freedom, lower values indicate a stronger balance between goodness-of-fit and parsimony (Akaike 2003; Caballero and Conesa 2005). Although deconvolution can resolve overlapped thermal events that are not separable by visual inspection, extracted components may remain sensitive to peak family, constraints, and initialization—especially under strong overlap or weakly expressed features—so information-criterion selection was interpreted alongside residual behavior and physically plausible bounds on peak position and width (Caballero and Conesa 2005; Kim et al. 2022). Figure 8 provides the stage-partition and diagnostic-point framework on a representative TG–DTG profile ($\beta = 10$ °C min^{-1}), visually linking the fixed boundaries in Table S8 to the experimental profiles used in subsequent analyses. Across heating rates, AIC/BIC selection indicates β-dependent statistical resolvability: a two-peak model is retained at $\beta = 5$ and 10 °C min^{-1}, whereas a three-peak model is preferred at $\beta = 20$ and 40 °C min^{-1} (Table S5).

Stage-resolved peak centers (μ) and normalized fractions (f_i) are summarized in Table S6, and the complete fitted parameter set (A, μ, σ, analytical area, f_i) is reported in Table S7. The deconvolution consistently identifies a dominant mid-temperature contribution ($\mu \approx 312–338$ °C; $f_i = 0.5005–0.9480$ depending on β; Table S6) and, where supported, a smaller high-temperature tail ($\mu \approx 465–491$ °C; $f_i = 0.0520–0.1188$; Table S6), Where a fitted component contributes negligibly resolved (e.g., $f_i \approx 1.8 \times 10^{-9}$ at $\beta = 20$ °C min^{-1}; Table S6), it is treated as statistically unsupported under the imposed constraints rather than interpreted as a distinct physical stage (Koga et al. 2023). For consistency across downstream diagnostics, fixed stage-boundary temperatures were used for segmentation ($b_1 = 150$ °C, $b_2 = 400$ °C for all β), as reported in Supplementary File S3 (Table S8).

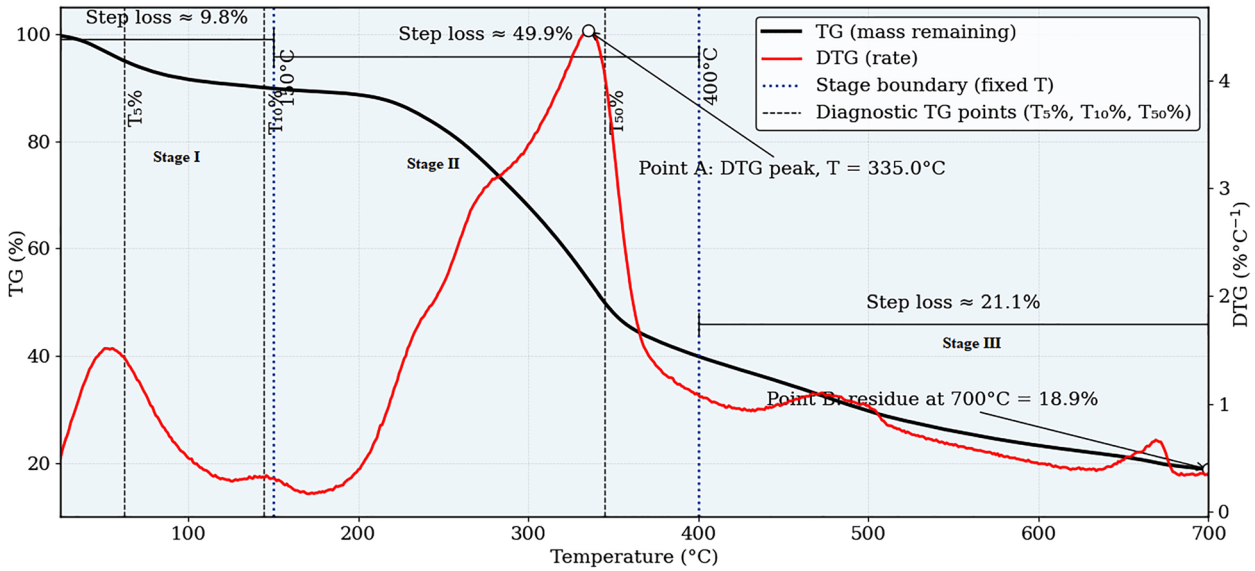

Fig. 8 TG–DTG profiles of raw lavender distillation residue under N_2 at 10 °C min^{-1} showing stage-resolved mass loss; boundaries (150, 400 °C), diagnostic points (T_5%, T_{10}%, T_{50}%), DTG peak (Point A), and residue at 700 °C (Point B) are indicated

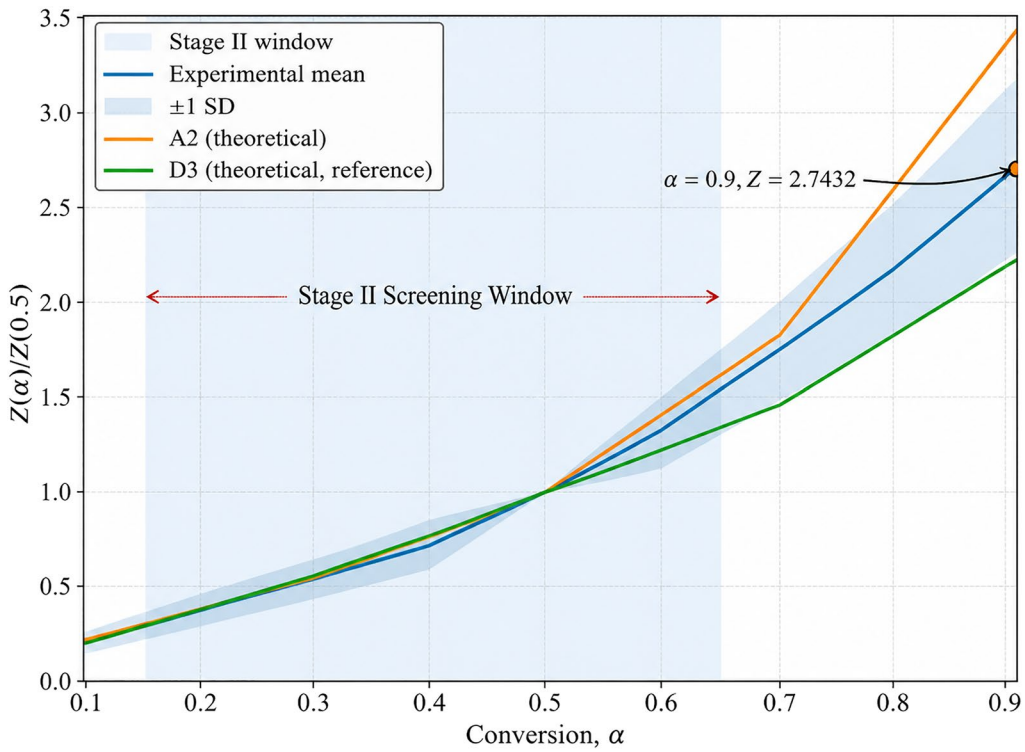

Fig. 9 Criado master plot showing experimental mean $Z(\alpha)/Z(0.5)$ (± 1 SD; $\beta = 5$–40 °C min^{-1}) with A2 best fit and D3 reference; Stage II window shaded

Reaction-mechanism screening was performed using the Criado master-plot framework, in which the experimental reduced-rate function $Z(\alpha)/Z(0.5)$ is compared with theoretical master curves representing idealized kinetic model families (Criado et al. 1989). Implementation descriptors are reported in Supplementary File S3 (Table S10), and the experimental master-plot values were aggregated across $\beta = 5$, 10, 20, and 40 °C min^{-1} and

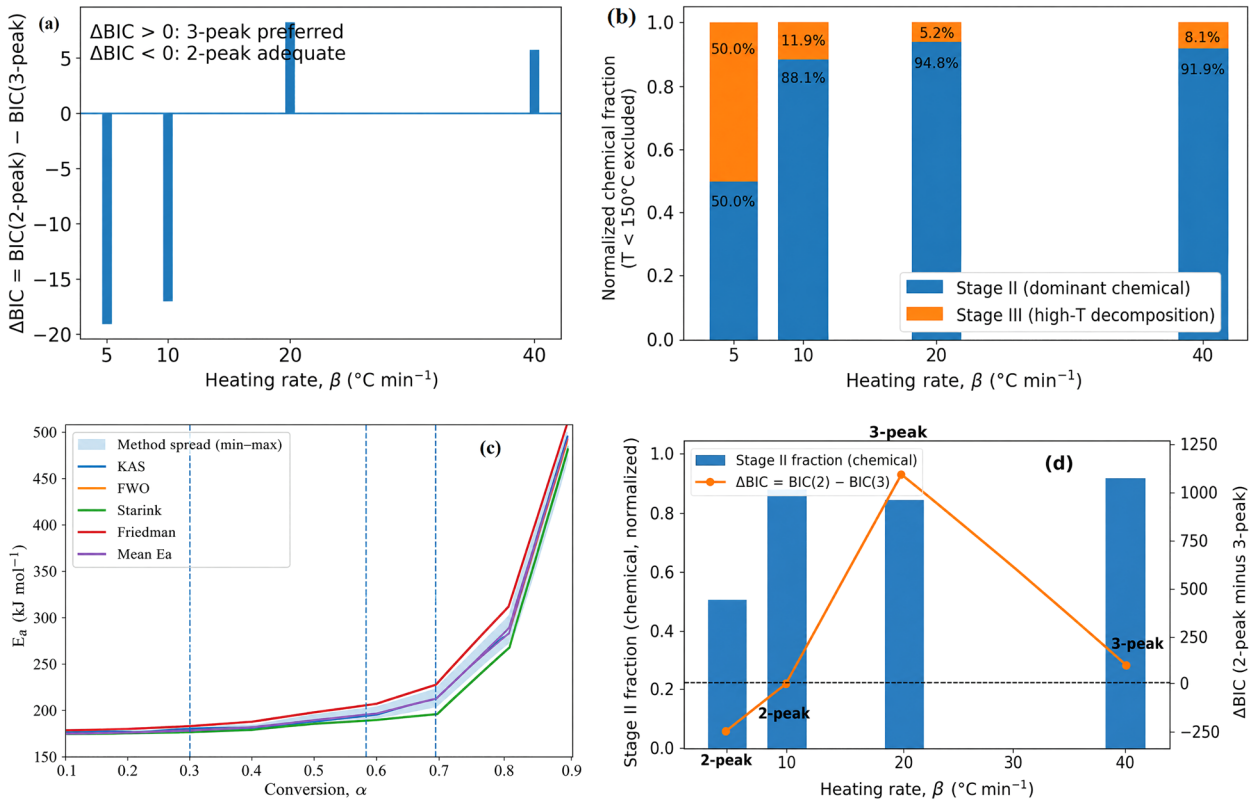

Fig. 10 Mechanism-resolved composite for lavender-residue pyrolysis across heating rates: **a** ΔBIC stage-count selection, **b** β-dependent stage contributions, **c** isoconversional $Ea(\alpha)$, and **d** integrated mechanism fingerprint summarizing regime-dependent kinetics

reported as mean ± SD (Table S11). As shown in Fig. 9, the experimental trajectory increases over $\alpha = 0.1$–0.9 from 0.1829 ± 0.0560 to 2.7432 ± 0.4712 (Table S11), indicating a strongly α-dependent reduced-rate signature. RMSE ranking identifies A2 as the closest-matching curve within the tested set both over the full α range ($RMSE_{all} = 0.2246$) and within the shaded Stage-II screening window ($RMSE_{stageII} = 0.1847$) (Table S12), with pointwise experimental–theory comparisons supporting this ranking at representative conversions (Table S13). Accordingly, the master-plot result is interpreted as a shape-consistency indicator within the tested model set, rather than evidence for a single elementary mechanism governing the full lignocellulosic pyrolysis pathway (Vyazovkin et al. 2011).

3.4 Mechanism-resolved analysis composite

Figure 10 integrates four complementary diagnostics—(a) information-criterion stage selection, (b) β-resolved DTG deconvolution fractions, (c) conversion-dependent isoconversional energetics, and (d) Criado master-plot screening—to interpret lavender-residue pyrolysis as a regime-evolving, multi-step pathway rather than a single global event. The underlying datasets are compiled in Supplementary File S3: Table S5 (RSS/AIC/BIC model selection), Tables S6–S7 (stage fractions and fitted peak parameters), Table S8 (stage-boundary temperatures), Table S9 ($Ea(\alpha)$ from KAS/FWO/Starink/Friedman), and Tables S10–S13 (Criado descriptors, experimental $Z(\alpha)/Z(0.5)$, RMSE ranking, and pointwise experimental–theory comparisons).

As shown in Fig. 10a, information criteria indicate that the devolatilization region is statistically best represented by two peaks at $\beta = 5$ and 10 °C min^{-1} but by three peaks at $\beta = 20$ and 40 °C min^{-1} (Table S5). This is reflected by $\Delta BIC = BIC_3 - BIC_2$ being positive at 5 and 10 °C min^{-1} (+19.06 and +17.00; favoring the 2-peak model) and negative at 20 and 40 °C min^{-1} (−8.24 and −5.72; favoring the 3-peak model). Because AIC and BIC are likelihood-based criteria that explicitly penalize added parameters, differences in these metrics are used to balance fit quality against model parsimony (Akaike 2003; Schwarz 1978). This β-dependence is therefore interpreted as heating-rate-dependent statistical resolvability under the adopted peak family/constraints, not as a literal count of elementary reactions; such fitted "components" in thermal-analysis signal decomposition are generally model-dependent and should be treated as phenomenological descriptors

unless independently validated (Koga et al. 2023; Vyazovkin et al. 2011).

Consistently, Fig. 10b (Tables S6–S7) shows a dominant mid-temperature contribution ($\mu \approx 312$–338 °C) plus a smaller high-temperature tail ($\mu \approx 465$–491 °C), with an additional low-μ component at higher β whose contribution is either minor ($\beta=40$) or effectively negligible ($\beta=20$). Specifically, at $\beta=5$ °C min^{-1} two peaks occur at $\mu=268.13$ °C ($f_i=0.4995$) and $\mu=325.66$ °C ($f_i=0.5005$); at $\beta=10$ °C min^{-1} two peaks occur at $\mu=312.20$ °C ($f_i=0.8812$) and $\mu=474.69$ °C ($f_i=0.1188$). Where three peaks are preferred, the mid-temperature component remains dominant ($\beta=20$: $\mu=325.60$ °C, $f_i=0.9480$; $\beta=40$: $\mu=338.49$ °C, $f_i=0.8264$) while the high-temperature tail persists as a smaller fraction ($\beta=20$: $\mu=465.10$ °C, $f_i=0.0520$; $\beta=40$: $\mu=491.17$ °C, $f_i=0.0730$). The additional low-μ component is negligible at $\beta=20$ ($\mu=129.26$ °C, $f_i=1.80\times10^{-9}$) but becomes non-negligible at $\beta=40$ ($\mu=78.36$ °C, $f_i=0.1006$). Because fitted peak count and component prominence can vary with heating program and with the chosen mathematical representation, the "Stage I/II/III" labels in Tables S6–S7 are treated as fitted components ordered by μ rather than fixed mechanistic stages (Koga et al. 2023; Vyazovkin et al. 2011). The energetic diagnostic in Fig. 10c (Table S9) is consistent with this regime evolution: apparent barriers are comparatively stable over $\alpha=0.1$–0.6 (KAS/FWO/Starink: 172.912–182.801 kJ mol^{-1}; Friedman: 175.588–191.744 kJ mol^{-1}), followed by a high-conversion shift where $E_a(\alpha)$ increases and uncertainty becomes more pronounced—most clearly for Friedman at $\alpha=0.7$ ($R^2=0.732$)—and Ea rises sharply at $\alpha=0.8$–0.9 (e.g., KAS 263.103→498.054 kJ mol^{-1}; Friedman 290.822→504.230 kJ mol^{-1}), consistent with late-stage carbonization/structural rearrangement where rates are low and derivative-based estimates become more sensitive to experimental noise and baseline/DTG differentiation effects (Friedman 1964; Vyazovkin et al. 2011). The isoconversional methods applied here are standard non-isothermal, model-free approaches widely used for solid-state decomposition kinetics (Akahira and Sunose 1971; Flynn and Wall 1966; Ozawa 1965).

Finally, the mechanism "fingerprint" in Fig. 10d shows that the experimental reduced-rate function $Z(\alpha)/Z(0.5)$ increases monotonically across $\alpha=0.1$–0.9 (Table S11), and RMSE screening identifies A2 as the closest-matching model family both over the full range ($RMSE_{all}=0.2246$) and within the Stage-II screening window ($RMSE_{stageII}=0.1847$) (Table S12), with pointwise comparisons supporting this ranking (Table S13). This master-plot approach follows the Criado reduced-rate formalism developed for discriminating among candidate solid-state kinetic model families by shape comparison (Criado et al. 1989), and the outcome is therefore used as a shape-consistency indicator within the tested model set rather than as proof of a single global elementary mechanism (Vyazovkin et al. 2011, 2014). Overall, the converging evidence across Fig. 10a–d supports interpreting lavender-residue pyrolysis as a multi-step, regime-evolving pathway: β-dependent resolvability of DTG sub-structure (two vs three components), a dominant mid-temperature devolatilization contribution plus a smaller high-temperature tail, a strong late-conversion escalation in $E_a(\alpha)$, and an A2-consistent reduced-rate signature. Together, these diagnostics support selecting operating windows using explicit decision criteria (e.g., yield/fixed-carbon targets alongside energy/LCA penalties) rather than asserting a single universal "optimum."

4 Conclusions

This study developed a mechanism-resolved framework for defining pyrolysis operating windows for lavender distillation residue by integrating DTG overlap diagnostics, conversion-dependent isoconversional kinetics, Criado master-plot screening, and energy/LCA-informed multi-criteria selection across a 13-run N_2 pyrolysis matrix. The results show that lavender-residue pyrolysis is a multi-step, regime-evolving process in which the preferred DTG representation depends on heating rate, while Ea remains relatively stable over $\alpha=0.1$–0.6 and rises sharply at high conversion, consistent with late-stage carbonization and structural rearrangement. Final temperature was the dominant control on the yield–carbonization trade-off. Within the explored design space, entropy-weighted TOPSIS identified Run 5 as the best-compromise condition (48.94% yield, 0.85 kWh kg^{-1} char, 2.05 kWh kg^{-1} fixed C), whereas Run 4 was preferred when a fixed-carbon constraint of FC ≥ 60% was applied. A limitation of the present study is that the energy analysis was based on furnace-rated electricity input as an upper-bound proxy and the environmental assessment was restricted to a gate-to-gate boundary; therefore, future work should include direct process-energy measurements, scale-up validation, and application-specific evaluation of the produced biochars. Overall, the framework provides a reproducible basis for more defensible and application-oriented operating-window selection for lavender-residue biochar valorization.

Supplementary Information

The online version contains supplementary material available at https://doi.org/10.1007/s42773-026-00617-9.

Additional file 1.

Additional file 2.

Additional file 3.

Acknowledgements
The authors gratefully acknowledge the support of the ECO-SPHERE MSCA COFUND Programme, co-funded by the European Union's Horizon Europe research and innovation programme under the Marie Skłodowska-Curie grant agreement No. 101126655 and by the Scientific and Technological Research Council of Türkiye (TÜBİTAK) under grant number 123C459.

Author contributions
Ahsanullah Soomro: Conceptualization, Methodology, Visualization, Investigation, Writing—original draft, Writing—review and editing. Anıl Tevfik Koçer: Methodology, Investigation, Formal analysis, Writing—original draft, Writing—review and editing. Mahdi Hassan: Visualization, Investigation. Didem Balkanlı: Supervision, Writing—review and editing. All authors read and approved the final manuscript.

Funding
This project has received funding fromthe European Union's Horizon Europe research and innovation program under the Marie Skłodowska-Curie grant agreement No.101126655. This project is also supported in part by a research grant from the Scientific and Technological Research Council ofTürkiye (TÜBİTAK) under grant number 123C459.

Data availability
All data supporting the findings of this study are available from the corresponding author upon reasonable request.

Declarations

Ethics approval and consent to participate
Not applicable. This study involved no human participants or animal experiments.

Declaration of generative AI and AI-assisted technologies in the writing process
During the preparation of this manuscript, the author(s) used ChatGPT (OpenAI) to improve language clarity and to refine the description and presentation of the modelling methodology (e.g., equations and calculation workflow). All analyses and numerical calculations were performed and verified by the authors, who reviewed and edited the text and take full responsibility for the content.

Competing interests
The authors declare that they have no competing interests.

Author details
[1]Department of Bioengineering, Yildiz Technical University, 34220 Istanbul, Turkey. [2]Department of Environment Engineering, Quaid-E-Awam University of Engineering, Science and Technology (QUEST), Nawabshah, Sindh, Pakistan. [3]Health Biotechnology Joint Research and Application Center of Excellence, 34220 Istanbul, Turkey. [4]Department of Environment Engineering, Yildiz Technical University, 34220 Istanbul, Turkey.

Received: 8 February 2026 Revised: 3 April 2026 Accepted: 8 April 2026
Published online: 03 June 2026

References

Aboyade AO, Görgens JF, Carrier M, Meyer EL, Knoetze JH (2013) Thermogravimetric study of the pyrolysis characteristics and kinetics of coal blends with corn and sugarcane residues. Fuel Process Technol 106:310–320
Agrawal A, Chakraborty S (2013) A kinetic study of pyrolysis and combustion of microalgae *Chlorella vulgaris* using thermo-gravimetric analysis. Bioresour Technol 128:72–80
Akahira T, Sunose T (1971) Method of determining activation deterioration constant of electrical insulating materials. Res Rep Chiba Inst Technol (Sci Technol) 16:22–31
Akaike H (2003) A new look at the statistical model identification. IEEE Trans Autom Control 19:716–723
Atinafu DG, Choi JY, Nam J, Kang Y, Kim S (2025) Insights into the effects of biomass feedstock and pyrolysis conditions on the energy storage capacity and durability of standard biochar-based phase-change composites. Biochar 7:18
Barar A, Bensebia O (2025) Surfactant assisted extraction for the recovery of bioactive compounds from solid wastes of lavender (*Lavandula angustifolia* Mill): optimization by Box-Behnken design. Process Biochem 153:170–181
Behzadian M, Otaghsara SK, Yazdani M, Ignatius J (2012) A state-of-the-art survey of TOPSIS applications. Expert Syst Appl 39:13051–13069
Caballero JA, Conesa JA (2005) Mathematical considerations for nonisothermal kinetics in thermal decomposition. J Anal Appl Pyrolysis 73:85–100
Cai W, Wang X, Zhu Z, Kumar R, Amaniampong PN, Zhao J, Hu Z-T (2023) Synergetic effects in the co-pyrolysis of lignocellulosic biomass and plastic waste for renewable fuels and chemicals. Fuel 353:129210
Chen K, Chen Y, Qi J, Xie J, Huang X, Jiang Y, Zhang S, Jia S, Chen Q, Xiao H (2023) Thermal degradation and curing kinetic study of urea formaldehyde/L-tyrosine composites. Int J Adhes Adhes 127:103493
Chen P (2021) Effects of the entropy weight on TOPSIS. Expert Syst Appl 168:114186
Chu G, Zhao J, Chen F, Dong X, Zhou D, Liang N, Wu M, Pan B, Steinberg CE (2017) Physi-chemical and sorption properties of biochars prepared from peanut shell using thermal pyrolysis and microwave irradiation. Environ Pollut 227:372–379
Criado J, Malek J, Ortega A (1989) Applicability of the master plots in kinetic analysis of non-isothermal data. Thermochim Acta 147:377–385
Crișan I, Ona A, Vârban D, Muntean L, Vârban R, Stoie A, Mihăiescu T, Morea A (2023) Current trends for lavender (*Lavandula angustifolia* Mill) crops and products with emphasis on essential oil quality. Plants 12:357
Desjardins SM, Ter-Mikaelian MT, Chen J (2024) Cradle-to-gate life cycle analysis of slow pyrolysis biochar from forest harvest residues in Ontario, Canada. Biochar 6:58
Dira A, Elmouwahidi A, Khouja S, Boufetacha M, Barakat A, Tayibi S, Carrasco-Marin F, Gharibi E (2024) Feedstock type and pyrolysis temperature of rosemary wastes in a fixed-bed reactor affect the characteristics and application potentials of the bio-chars. J Anal Appl Pyrolysis 182:106697
Enebe MC, Ray RL, Griffin RW (2025) The impacts of biochar on carbon sequestration, soil processes, and microbial communities: a review. Biochar 7:107
Ferfari O, Belaadi A, Alshahrani H, Ghernaout D, Mukalazi H (2025) Unraveling the pyrolysis mechanisms of *Syagrus* palm waste fibers through Gaussian deconvolution and kinetic modeling. J Nat Fibers 22:2562473
Flynn JH, Wall LA (1966) A quick, direct method for the determination of activation energy from thermogravimetric data. J Polym Sci B Polym Lett 4:323–328
Fraga LG, Silva J, Teixeira S, Soares D, Ferreira M, Teixeira J (2020) Influence of operating conditions on the thermal behavior and kinetics of pine wood particles using thermogravimetric analysis. Energies 13:2756
Friedman HL (1964) Kinetics of thermal degradation of char-forming plastics from thermogravimetry. Application to a phenolic plastic. J Polym Sci C Polym Symp 6:183–195
Gamaralalage D, Rodgers S, Gill A, Meredith W, Bott T, West H, Alce J, Snape C, McKechnie J (2025) Biowaste to biochar: a techno-economic and life cycle assessment of biochar production from food-waste digestate and its agricultural field application. Biochar 7:50
García R, Pizarro C, Lavín AG, Bueno JL (2012) Characterization of Spanish biomass wastes for energy use. Bioresour Technol 103:249–258
Gotor FJ, Criado JM, Malek J, Koga N (2000) Kinetic analysis of solid-state reactions: the universality of master plots for analyzing isothermal and nonisothermal experiments. J Phys Chem A 104:10777–10782
Karagianni A-G, Paraschou A, Matsi T (2025) A preliminary evaluation of the use of solid residues from the distillation of medicinal and aromatic plants as fertilizers in Mediterranean soils. Agronomy 15:1903
Khawam A, Flanagan DR (2006) Solid-state kinetic models: basics and mathematical fundamentals. J Phys Chem B 110:17315–17328
Kim H, Yu S, Kim M, Ryu C (2022) Progressive deconvolution of biomass thermogram to derive lignocellulosic composition and pyrolysis kinetics for parallel reaction model. Energy 254:124446
Kissinger HE (1957) Reaction kinetics in differential thermal analysis. Anal Chem 29:1702–1706

Koçer A, Özçimen D (2022) Experimental investigation on thermal behavior and thermo-kinetic study on pyrolysis of de-oiled microalgae. Int J Environ Sci Technol 19:12279–12288
Koçer AT, Erarslan A, Özçimen D (2023) Pyrolysis of *Aloe vera* leaf wastes for biochar production: kinetics and thermodynamics analysis. Industrial Crops and Products 204:117354
Koçer AT, Karacaoğlu B, Karaca GA, İnan B, Balkanlı D (2024) Thermal behavior analysis and biochar formation through co-pyrolysis of de-oiled microalgae biomass and wood sawdust for ecofriendly resource utilization. Algal Res 82:103674
Koçer AT, Mutlu B, Özçimen D (2020) Investigation of biochar production potential and pyrolysis kinetics characteristics of microalgal biomass. Biomass Conv Bioref 10:85–94
Koga N, Vyazovkin S, Burnham AK, Favergeon L, Muravyev NV, Pérez-Maqueda LA, Saggese C, Sánchez-Jiménez PE (2023) ICTAC Kinetics Committee recommendations for analysis of thermal decomposition kinetics. Thermochim Acta 719:179384
Lesage-Meessen L, Bou M, Ginies C, Chevret D, Navarro D, Drula E, Bonnin E, Del Río JC, Odinot E, Bisotto A (2018) Lavender- and lavandin-distilled straws: an untapped feedstock with great potential for the production of high-added value compounds and fungal enzymes. Biotechnol Biofuels 11:217
Li X, Baran SS, Orange F, Bonjour E, Jame P, Verger-Dubois G, Mija A, Lomenech C, Kuzhir P, Hurel C (2023a) Conversion of *Lavandula* straw into high-quality solid fuel: effect of hydrothermal carbonization conditions on fuel characteristics. BioEnergy Res 16:1156–1172
Li X, Liu H, Liu N, Sun Z, Fu S, Zhan X, Yang J, Zhou R, Zhang H, Zhang J (2023b) Pyrolysis temperature had effects on the physicochemical properties of biochar. Plant Soil Environ 69:8
Lindstrom JK, Peterson CA, Ciesielski PN, Ralph J, Chen M, Jakes JE, Johnston PA, Rollag SA, Brown RC (2024) Structural and chemical changes in hardwood cell walls during early stages of flash pyrolysis. Front Energy Res 12:1348464
Logeshwari G, Jeyashri K, Rajkumar M, Manikandan H, Sivakumar K, Selvanayagam S, Rajathi V (2024) Benzylidene-isophorone hybrids with strong anticancer activity. Spectrochim Acta A Mol Biomol Spectrosc 319:124577
Montoya J, Pecha B, Janna FC, Garcia-Perez M (2017) Identification of the fractions responsible for morphology conservation in lignocellulosic pyrolysis: visualization studies of sugarcane bagasse and its pseudo-components. J Anal Appl Pyrolysis 123:307–318
Nhuchhen DR (2016) Prediction of carbon, hydrogen, and oxygen compositions of raw and torrefied biomass using proximate analysis. Fuel 180:348–356
Oginni O, Singh K (2020) Influence of high carbonization temperatures on microstructural and physicochemical characteristics of herbaceous biomass derived biochars. J Environ Chem Eng 8:104169
Ozawa T (1965) A new method of analyzing thermogravimetric data. Bull Chem Soc Jpn 38:1881–1886
Özçimen D, Ersoy-Meriçboyu A (2010) Characterization of biochar and bio-oil samples obtained from carbonization of various biomass materials. Renew Energy 35:1319–1324
Parikh J, Channiwala S, Ghosal G (2005) A correlation for calculating HHV from proximate analysis of solid fuels. Fuel 84:487–494
Parvari E, Mahajan D, Hewitt EL (2025) A review of biomass pyrolysis for production of fuels: chemistry, processing, and techno-economic analysis. Biomass 5:54
Permana D, Atmaja L, Priyangga A, Ivana Kedang YI, Santoso M (2024) Utilization of cellulose-based carbon nanodots in sulfonated polysulfone based membrane for direct methanol fuel cell. S Afr J Chem Eng 48:265–275
Poomsawat S, Poomsawat W (2021) Analysis of hydrochar fuel characterization and combustion behavior derived from aquatic biomass via hydrothermal carbonization process. Case Stud Therm Eng 27:101255
Porcu A, Xu Y, Mureddu M, Dessì F, Shahnam M, Rogers WA, Sastri BS, Pettinau A (2021) Experimental validation of a multiphase flow model of a lab-scale fluidized-bed gasification unit. Appl Energy 293:116933
Ravindiran G, Rajamanickam S, Janardhan G, Hayder G, Alagumalai A, Mahian O, Lam SS, Sonne C (2024) Production and modifications of biochar to engineered materials and its application for environmental sustainability: a review. Biochar 6:62
Rego F, Dias APS, Casquilho M, Rosa FC, Rodrigues A (2019) Fast determination of lignocellulosic composition of poplar biomass by thermogravimetry. Biomass Bioenergy 122:375–380
Schomberg AC, Bringezu S, Flörke M, Biederbick H (2022) Spatially explicit life cycle assessments reveal hotspots of environmental impacts from renewable electricity generation. Commun Earth Environ 3:197
Schwarz G (1978) Estimating the dimension of a model. Ann Stat 6:461–464
Sharma P, Bilican A, Schmidt W, Ochoa-Hernández C, Etter M, Weidenthaler C (2024) Nitrogen doping in carbon xerogels via ammonia pyrolysis: a case study. Mater Today Chem 40:102238
Shrivastava P, Palamanit A, Kumar A (2025) Isoconversional thermal decomposition reaction kinetics of oil palm trunk and rubberwood sawdust for thermochemical conversion processes. Environ Sci Pollut Res 32:19015–19025
Starink M (1996) A new method for the derivation of activation energies from experiments performed at constant heating rate. Thermochim Acta 288:97–104
Su S, Tahir MH, Cheng X, Zhang J (2024) Modification and resource utilization of coal gasification slag-based material: a review. J Environ Chem Eng 12:112112
Syguła E, Ciolkosz D, Białowiec A (2024) The significance of structural components of lignocellulosic biomass on volatile organic compounds presence on biochar-a review. Wood Sci Technol 58:859–886
Tariq I, Hassan H, Ali S, Raza SA, Shah PA, Ali MY, Tariq Z, Bakowsky U (2024) Ameliorative delivery of docetaxel and curcumin using PEG decorated lipomers: a cutting-edge in-vitro/in-vivo appraisal. J Drug Deliv Sci Technol 97:105814
Vyazovkin S, Burnham AK, Criado JM, Pérez-Maqueda LA, Popescu C, Sbirrazzuoli N (2011) ICTAC Kinetics Committee recommendations for performing kinetic computations on thermal analysis data. Thermochim Acta 520:1–19
Vyazovkin S, Chrissafis K, Di Lorenzo ML, Koga N, Pijolat M, Roduit B, Sbirrazzuoli N, Suñol JJ (2014) ICTAC Kinetics Committee recommendations for collecting experimental thermal analysis data for kinetic computations. Thermochim Acta 590:1–23
Wang L, Lei H, Liu J, Bu Q (2018) Thermal decomposition behavior and kinetics for pyrolysis and catalytic pyrolysis of Douglas fir. RSC Adv 8:2196–2202
Yang H, Yan R, Chen H, Lee DH, Zheng C (2007) Characteristics of hemicellulose, cellulose and lignin pyrolysis. Fuel 86:1781–1788
Yılmaz Çinçin RG, Öngen A, Ağdağ ON (2025) Essential oil distillation residue as environmentally friendly feedstock in gasification: effect of dry air flow rate and temperature on gasification performance. Biomass Conv Bioref 15:11719–11733
Zhang X, Zhang P, Yuan X, Li Y, Han L (2020) Effect of pyrolysis temperature and correlation analysis on the yield and physicochemical properties of crop residue biochar. Bioresour Technol 296:122318
Zhang Z, Zhang C, Sun B, Xu X, Chen X, Li Z, Wang S (2025) Synergistic effect in the co-pyrolysis of lignin and petrochemical heavy oil: kinetic characteristics and product composition. J Energy Inst. https://doi.org/10.1016/j.joei.2025.102306
Zhu H, Yi B, Hu H, Fan Q, Wang H, Yao H (2021) The effects of char and potassium on the fast pyrolysis behaviors of biomass in an infrared-heating condition. Energy 214:119065